2021 43rd Annual International Conference of the
IEEE Engineering in Medicine & Biology Society (EMBC)
Oct 31 - Nov 4, 2021. Virtual Conference

Development on Linearizing Front End and Amplification Structure for Commercial GMR Sensor-based Cardiorespiratory Monitoring system

Sayan Sarkar[1], Tamaghno Chatterjee and Aayushman Ghosh

***Abstract*— Magnetoplethysmogram (MPG) is typically acquired by placing a giant magnetoresistance sensor (GMR)-magnet system in a blood vessel's (e.g., radial artery) vicinity. This brief analyzed multiple linearizing front ends for the GMR-magnet system. GMR based analog front end's (AFE) gain requirement is derived through COMSOL and MATLAB-based simulation considering the raw signal data. After that, we designed a fully differential difference amplifier (FDDA) in 0.18 µm, 1.8 V process using the SPICE environment for amplification of MPG signals. An automatic calibration method is used for compensating the GMR sensor's offset and lowering it to a few µV level during constant current excitation. This proposed GMR-magnet system is a stepping stone towards non-invasive arterial pulse waveform (APW) detection using the MPG principle, with or without direct skin contact. The DDA achieves open and closed-loop gain of 102 dB and 32 dB, phase margin of 62°, an IRN of 1.8µV, and a unity-gain frequency of 32kHz, resulting in a closed-loop bandwidth of 800 Hz while dissipating 1.2 µA from a 1.8-V supply.**

I. Modelling of the Magnetic Field

Magnetoplethysmogram (MPG) is realized by exposing a body part (preferably with arterial vessels close to the skin tissues) with a magnetomotive force (MMF) and checking the resultant flux with a sensor [1]-[3]. The MMF produced by the permanent magnet generates a magnetic flux (ϕ)[4]-[9], that depends on the cumulative reluctance (R_T) of the magnetic path ($\phi = MMF/R_T$) [1]-[3]. Total reluctance [9] of the equivalent magnetic path consists of: reluctance of (i) permanent magnet (R_M), (ii) flux sensor device (R_S), (iii) air path (R_A) (iv) skin-tissue (R_{ST}) and (v) blood vessels ($R_B(t)$). The reluctance offered by the magnet, skin tissue, and the air is constant with time [9]. The blood vessels' reluctance varies with the change in blood volume flowing through the blood vessels [4]. Net reluctance (R_T) of the equivalent magnetic path of the MPG sensor head follows (1) [9].

$$R_T = R_M + R_A + R_S + R_{ST} + R_B(t) \tag{1}$$

The reluctance R_F of the equivalent magnetic path in (2) through magnet, sensor, air, and tissue ($R_F = R_M + R_A + R_S + R_{ST}$) is fixed [9].

$$R_F = \frac{l_R}{\mu_R A} \tag{2}$$

Here, l_R is the equivalent path length of the constant reluctance R_F, and μ_R is the equivalent permeability of that path [9]. If M_m is the magnetomotive force (MMF) generated by the magnet, the flux ϕ picked up by the flux sensor follows (3), according to the condition $R_F >> R_B(t)$ [9].

$$\phi = \frac{M_m}{(R_F + R_B(t))} = \frac{M_m}{R_F}\left(1 - \frac{R_B(t)}{R_F}\right), R_B(t) = \frac{l_B(t)}{\mu_B A} \tag{3}$$

In (3), $l_B(t)$ is the flux path length hold by blood and μ_B is the permeability of blood. Magnetic field follows (4) [9].

$$B_{mod} = \frac{\phi}{A} = \frac{M_m}{R_F A}\left(1 - \frac{\mu_R l_B(t)}{\mu_B l_F}\right) = B_{fixed}(1-x) \tag{4}$$

The GMR sensor comprises four GMR elements [1]-[11], arranged in a bridge format. Two GMR elements (R_o) in the network are passive. whereas other two GMR elements (R_G) vary with the input magnetic field (say, B_{mod}), as per (5). Due to the repeated changes in blood volume and $R_B(t)$, B_{fixed} magnetic field changes to B_{mod}.

$$R_G = R_{OL}\left(1 - K_s\left(B_{mod} - B_L\right)\right) \tag{5}$$

By Combining (4) and (5), we get the magnetic field and GMR element resistance variation relationship in (6). Multiple works are carried out based on the above formulation of resistance variation with incident magnetic field [5]-[9] but combining mathematical modeling, COMSOL simulation, and SPICE-based analysis for AFE design is still in its nascent stage [17]-[18]. Optimizing the GMR sensor probe decreases the complexity and power budget of the signal conditioning electronics. Recent literature worked on the optimal distance between the GMR sensor and magnet [4]. At sub-optimal GMR sensor-magnet interaction, the amplification factor will increase [4]. We handpicked available GMR linearization circuits [4]-[7] and thoroughly analyzed their gain requirement, structure complexity, and power consumption.

$$R_G = R_{OL}\left[1 - K_s\left(B_{fixed} - B_L\right)\right] + xK_s B_{fixed} R_{OL} \tag{6}$$

II. Excitation of the GMR Sensor

GMR sensor can be excited either by a constant current source [1],[7],[18], or a fixed voltage source [2],[3]. Current source-based excitation has advantages like better SNR, low power consumption over voltage-based excitation [1]. Scheme 1 follows Fig.1 [4]. V_R and R_C are the precision reference voltage (from band-gap reference) and an off-chip fixed resistor. R_C gives the current I_C through the GMR sensor as per $I_c = V_c/R_c$. The current I_C gets divided equally into two paths of the bridge in the absence of any offset. In this way, the current drawn by the bridge can be controlled by the designer [4]-[7], which is important for power consumption reduction. The differential output voltage V_{GMR} from the GMR sensor follows (7) [7]. The output voltage of the

[1]Sayan Sarkar, Tamaghno Chatterjee, Aayushman Ghosh are with Wecare Medservice LLP, Kolkata, India
wecaremedservicellp@gmail.com

sensor V_{GMR} is amplified using an instrumentation amplifier (A_I) having a gain of K_I [7]. The amplified output voltage follows (8). During on-chip implementation, supply voltage V_{DD} is small; subsequently, the maximum voltage across the GMR sensor is bounded to V_{AB} (node A and node B voltage difference). If the maximum output voltage of A_C is V_{DD}, then $V_{AB(max)} \approx (V_{DD} – V_R)$. This voltage limits the maximum I_C and its operating range [5]-[7].

$$V_{GMR} = \frac{I_C}{2}(R_O - R_G) = \frac{V_R}{2R_C}(R_O - R_G) \tag{7}$$

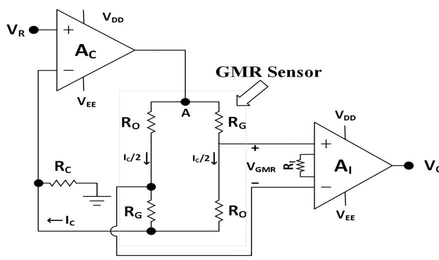

Fig. 1. Constant current based excitation [9]

$$V_O = A_I \frac{K_s R_o V_R[(B_f - B_L) - xB_f]}{2R_c} \tag{8}$$

In scheme 2, the biasing circuit of the GMR sensor has a V-to-I converter [9] based on Fig.2. It uses a single-stage differential amplifier topology as stage 1 and a common-source PMOS amplifier (M_1) with an R_C resistive load [7],[22]. The Miller-compensation (C_F and R_Z) provides the negative feedback loop's stability [7]. The M_1 - M_2 transistor pair works as a current mirror circuit. This scheme has reduced the non-linearity of the system [7]. Output voltage is modified to (9) w.r. t (8) in new configuration [9].

$$V_O = V_R[1 + A_I \frac{K_s R_o[(B_f - B_L) - xB_f]}{2R_c}] \tag{9}$$

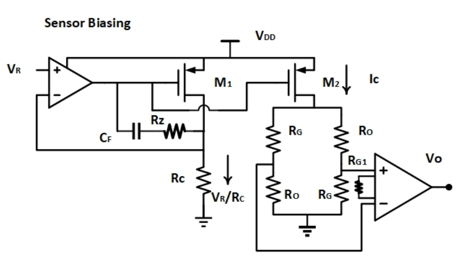

Fig. 2. Modified Constant current based excitation [12]

III. Estimation of the Magnetic Field

The applied magnetic field surrounds the GMR sensor, skin, fabric, and blood vessels [7]-[9]. The distance between GMR and magnet is important to achieve magnetic biasing's desired effect. We calculated the magnetic field by importing device parameters of sensor and magnet [10] in the MATLAB environment. During the estimation, the permanent magnet is assumed to be a point source. The magnetic field (B) along its axis, at a distance (d) away from the point source, follows (10) [8].

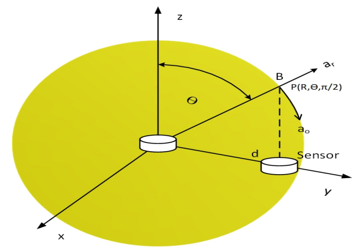

Fig. 3. Magnetic field calculation

$$B = \frac{\mu_o M}{4\pi d^3}(a_R 2\sin\theta + a_\theta \cos\theta) \tag{10}$$

Where, μ_o is the permeability of the equivalent magnetic path, d is the distance of the sensor from the centre of the magnet, a_R and a_θ are standard unit vectors and M is the magnetic moment vector. Applying $\theta = 90°$ in (10), the magnetic field (B) follows (11) [4]-[9] as per Fig.3.

$$B = \frac{\mu_o M}{4\pi d^3} a_\theta \tag{11}$$

As per the datasheet, the sensor-magnet are AA004-02 and D125B, respectively. Magnetic moment of the magnet $\approx$ 0.05 A m^2. The magnetic field strength (B) at d = 20 mm from the sensor is 0.625 mT [8]. This magnetic field strength is the worst possible magnetic field without any field concentrator. However, it produces the desired effect of magnetic biasing when the sensor operates in its characteristic curve's linear region [5]-[9]. The linear range of AA004-02 sensor lies within 0.5 – 3.5 mT. Properties of the GMR sensor and magnet combinations are listed in Table I. We co-simulated the available GMR sensor in COMSOL and MATLAB environment [2] with different magnets for limiting distance and typical sensor output calculation with 5 V supply voltage for off-chip implementation. These values are important for calculation of AC/DC signal ratio and amplifier gain [9]. We ignored the magnetic field calculation for literature [8] in Table II because the same category (N35) magnet is used in [1],[13],[22] by modifying the dimension. Based on Table II, the best possible combination for GMR based wearable implementation is AA004-02 GMR sensor and N40 (D125B) magnet. Recent research works [2]-[3],[9] have opened different configurations for signal conditioning like (i) the sensor-magnet distance is 20 mm without a magnetic field concentrator [1],[13]; (ii) sensor-magnet distance is 12 mm with a field concentrator [2]. A magnetic field concentrator prevents the bulging effect of the flux lines, but it is not helpful for compact wearable realization. In the'best possible bio-magnetic field available at 12 mm distance' case, researchers have committed some mistakes. The post-amplification high amplitude bio-signal [2] obtained in their case is due to improper biasing. As per literature [10], the linear operating region of AAH002-02 sensor lies in between -50 - +50 mT [2],[3],[9] but actually operating region lies within 0.06-0.3 mT [10]. The sensor is probably not biased at the linear operating region. Table II gives the limiting operating distance between sensor and magnet and corresponding magnetic field. Researchers [2] used a Neodymium magnet of 4 mm diameter and 3 mm thickness (D125B) during emulation in COMSOL environment [2]. As per studies [2],[3], the bio-magnetic field available to the sensor lies within 20-25 µT at an optimum distance of 12 mm with field concentrator. Another study [8] assumed 20 mm operating distance w/o field concentrator, supported by other literatures [1]-[3]. Our analysis is based on the 20 mm operating distance between sensor and magnet.

IV. DDA Design of the Front End

During AFE design for wearable [11]-[20], high input impedance, low noise, high common mode rejection ratio (CMRR), and ultra low power consumption are the most important performance indicators [14]-[16]. AC-coupled AFE [20] with auxiliary circuits, such as 'impedance boosting' and 'DC-servo loop', are not good candidate for the ultra-low-power signal interfacing. DC-coupled AFE shows inherent high input impedance but suffers with poor CMRR. DDA with modified DC-coupled AFE [19]-[20] is a suitable candidate featuring the inherent high input impedance, high CMRR, circuit simplicity, and low power consumption. At 20 mm distance between sensor and magnet, the best and worst possible DC magnetic field lies within 2.5mT and .625mT respectively [1]-[9],[15]. The lower threshold of the magnetic field (B_L) is .5mT [5]-[7]. Typically amplifier and GMR sensor biasing circuit are supplied from a single supply. As per different literature, the amplification factor lies within 1600 in extreme cases to prevent saturation of GMR signal [1],[13]. Total gain of the AFE is implemented in multiple stages (fixed and programmable gain amplifier). Biomagnetic field varies within 0.1-2µT based on COMSOL simulation in the vicinity of 20 mm distance [2]. During on chip implementation, 0.18 µm, 1.8 V CMOS process is used. The closed-loop configuration of the amplifier has capacitative gain and pseudo resistor (high-pass filter realization, cut-off frequency < 1 Hz) based structure [20]. Typically AA series commercial GMR sensor provides an offset of 4 mV/V [10]. At 1.8 V supply voltage and 5 kΩ reference resistance, system requires 0.72 µA compensation current [19]. During constant voltage excitation, the generated offsets at V_{in}+ and V_{in}- are symmetrical about common mode voltage. Whereas in constant current based excitation, offset voltage close to $I_B(\frac{r_L}{8}$-$\frac{r_R}{8})$ and $I_B(\frac{r_R}{8}$ + $\frac{3r_L}{8})$ exist at V_{in}+ and V_{in}-, respectively.The generated offsets are asymmetrical w.r.t common mode voltage. In GMR sensor, maximum difference between resistance variation (r_L-r_R) is found to be 12.4 Ω [7]. The offset generated at V_{in}+ node is µV level. So, the need of offset compensation is relaxed than voltage based excitation. However, an optional calibration unit based on 'intended use' is still kept in the system. In this design, V_R is 1.2 V and V_{DD} = 1.8 V. Considering $(R_O + R_G)$ = 10 kΩ, the design in Fig.4(a) gives I_C(max) = 1.8/10 mA = 180µA [7]. In this design, considering R_C = 24 kΩ, I_C is fixed at (1.2/24) mA = 50 µA based on SNR value close to 50 dB [1],[7]. This low current is reducing overall power consumption of the biasing circuit in µW level. An automatic calibration technique is used to nullify the resistive-bridge offset (caused by GMR and magnetic field variations) and reduce it to µV level [19]. System requires 0.2 µA compensation current [19]. MR sensors typically have higher no. of bits based DAC requirement for offset compensation [12]. Above analysis comprehends that constant current excitation reduces offset compensation current nearly 4x times w.r.t constant voltage based excitation. Subsequently, the DAC requirement is reduced by 2 bit (from 7 bit DAC- constant voltage excitation to 5 bit DAC- constant current excitation).

The bridge offset calibration circuit, in Fig. 4(a), adapted from [19] generates the compensation current automatically. It has two switches S_P and S_N and two 5-bit current DACs (I-DACs) with binary current units I_{P0}-I_{P4} and $I_{N0} - I_{N4}$, one comparator, and a SAR control unit. Each current source's current is developed from a temperature-insensitive current source supplied by a BGR (bandgap voltage reference). Performance of the I-DAC [19] is linked to the size and biasing condition of the transistors in the unit current source[21]. An integral non-linearity (INL) specification of ±0.5 LSB for 5-bit matching accuracy, the standard deviation of the unit current source should not be larger than 2.8% of the unit current [19],[21] to obtain a good yield. The sensor is calibrated in a one-time two-steps manner, and it reduces overall power consumption. The calibration process is triggered with a falling pulse on the 'start signal' in Figs.4(b) and (d) [19]. In the first step, S_N is on, and the clocked comparator compares the sensor's negative output, $V_{in}-$, with the common-mode level, V_{CM} [19]. The SAR logic generates codes D_{N0}–D_{N4} to adjust $V_{in}-$ through the I-DACs, I_{N0}–I_{N4}. As per Fig. 4(d), after seven clock cycles, $V_{in}- = V_{DD}$ - R×(I_L+I_N) approaches V_{CM}, and the first step is completed, where $\triangle \mathrm{I}_N = \sum_{i=0}^{4} \mathrm{D}_{Ni} \times I_{Ni}$. I_N is the current in the i_{th} current branch I_{Ni} = 2 × I_{Ni-1}, and i = 0 - 4. In the second step, S_N is off, S_P turns on (optional), then the comparator and SAR logic modify I-DACs[19]. I_{P0}–I_{P4} is generated in the same manner where $\triangle \mathrm{I}_P = \sum_{i=0}^{4} \mathrm{D}_P i \times I_{Pi}$. Finally, both S_P and S_N turn off, and I-DACs hold the compensation currents [19]. I_L and I_R are the currents through the left and right-hand sides of the bridge, respectively. After offset calibration, the calibration block is disabled to save power consumption until triggering of the 'START' signal [19]. The comparator in Fig. 4(b) consists of a preamplifier (preamp) followed by a strong-arm (SA) latch. The preamp can amplify the small input signal while the SA latch compares the amplified signal and provides the corresponding logic. The high gain preamp reduces the kickback noise and latch offset [19]. During the calibration, the control signal 'EN' goes low to enable the preamp. 'EN' stays at a high level to turn off the preamp for reducing power consumption. The SA latch has two phases: the RST phase (ϕ_C=1) and the comparison phase (ϕ_C = 0) [19], where the clock ϕ_C is synchronized with the SAR logic in the bridge-offset calibration circuit [19]. The latch has low power consumption because of no

TABLE I
MAGNETORESISTIVE SENSOR AND MAGNET PROPERTIES

Author	Sensor- Magnet Combination	Magnet specification		Surface flux measurement (T)	Residual flux density (KGs)
		Dia (cm)	Thickness (cm)		
Anoop [13]	AA004-02 N35(D063D)	1.27	0.16	0.1637	11.7-12.1
Kumar [4],[5]	AAH002-02 N40(D125B)	0.635	0.3175	0.3279	12.6-12.9
Sen [5],[6], [7]	AA004-02 No data	-	-	-	-
Phua [8]	AA004-02 N35(M1 219-4)	0.6	0.2	0.2500	11.7-12.1

TABLE II
COMPARATIVE ANALYSIS OF LIMITING DISTANCE FOR GMR-MAGNET SYSTEM

Sensor Name	Linear magnetic Field region(mT)	Limiting condition N35 (D063D)		Limiting condition N40 (D125B)		Sensor output @5V AA004-02-N40 (mV)
		magnetic field(mT)	distance(mm)	magnetic field(mT)	distance(mm)	
AA002	0.15-1.05	0.15	64.4	0.15	50.7	27
		1.05	33.2	1.05	25.7	192
AA004	0.5-3.5	0.5	43.1	0.5	33.4	28
		3.5	21.5	3.5	16.6	193
AAH002	0.06-0.3	0.06	86.5	0.06	68.6	44.8
		0.3	51.4	0.3	40.1	215

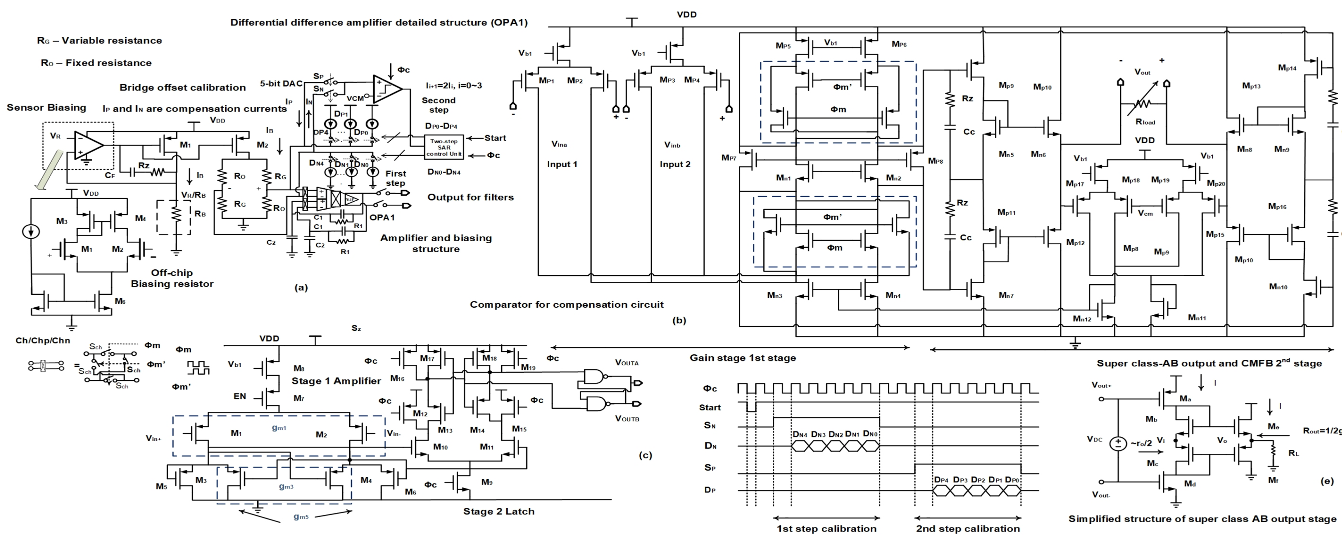

Fig. 4. (a) GMR based APW Monitoring IC, (b) Offset calibration circuit, (c) DDA and (d) timing diagram for calibration, (e) simplified super class AB output stage (adapted from [19])

static biasing. The SR latch stores the output from the SA latch for one clock cycle. The comparator consumes 250 nW. In DDA, the large-size input transistors (M_{P1}–M_{P4}) [14],[19] are used to improve the noise performance and offset. The parasitic capacitance C_{par} in the feedback network contributes to better consistency of gain without using extra area [20]. Unit size of transistor's is much smaller than the MIM capacitor, so higher numbers of symmetrically placed units are allowable for transistors than capacitors within the same area [20]. The capacitor area of C_2 is reduced since part of capacitance is provided by C_{par} (parasitic capacitor reusing) at C_2 [20]. The parasitic capacitance contributes about 1/5 of the gain as per simulation, i.e., the ratio of C_{par} and C_2 is around 1/4 in the CMOS process. The reuse of C_{par} improves CMRR and noise performance. The impedance at DC is targeted at GΩ range in this design, so C_{par} can't be too large. The designed FDDA has high DC gain, a high-pass cut-off frequency of $1/(2\pi \times R_1 \times C_1)$, and mid-band gain of $(C_2+C_{par}+C_1)/C_1$. R_1 is a back-to-back connected pseudo resistor which is several GΩ [20]. Four switches form the chopper modulators (ch/chn/chp) for input noise reduction in Fig. 4(a). The chopper modulators are driven by non-overlapping clocks ϕ_m and ϕ_m' at 20kHz frequency [19]. The DDA utilizes capacitative feedback composed of C_1 and C_2 to achieve a differential gain of 32 dB. The DDA isolate the compensation currents from the I-DACs due to high input impedance. Fig. 4(c) shows the schematic of the core amplifier OPA_1 with a folded-cascode dual-input stage M_{P1}-

TABLE III
COMPARATIVE ANALYSIS OF EXISTING STATE OF THE ART AMPLIFIER

Author Conference	Zuo[18] ISCAS	Cabrera[16] TCAS I	Ayman[12] SENSORS	Oreggioni[15] TBIOCAS	Zhao[20] TBIOCAS	Zuo[17] ICECS	Hsu[19] JSSC	This work (Simulated)
Voltage supply	1.8 V	1.2 V	1.8 V	3.3 V	1.8 V	1.8 V	1.8 V	1.8 V
Process	0.18μm	0.13μm	0.18μm	0.5μm	0.35μm	0.18μm	0.18μm	0.18μm
Power dissipation(μW)	0.288	35.8	-	28	0.63	58	1.98	2.16
UGF(MHz)	3.8	0.011	> 60	0.4	0.36	0.5	0.01	0.032
Open loop DC gain (dB)	118	40	60	49.2	75	80	110	102
IRN (μV_{rms})	-	1.3	-	1.88	1.02	1.41	5.84	1.8
Noise BW (KHz)	0.1	100	-	25	0.12	1	0.1	0.1
Phase Margin(degree)	60.6	-	-	-	-	62.5	65	62
CMRR(dB)	136.62	86	-	85	76	102	80	84
Amplifier Topology	FC CMFB	Modified CMFB	Fully DDA DDA	DDA -	Fully DDA	FC CMFB	Fully DDA CMFB	Fully DDA CMFB
NEF, PEF	-	2.5,7.5	-	2.1,14.6	1.98,6.42	-	10.54,34.15	2.68, 8.68

M_{P4} and a super class-AB output stage [19]. Miller capacitors C_C is used for frequency compensation whereas resistor R_Z is used to avoid the RHP zero. The CMFB circuit senses the output voltage at $V_{out}-$ and $V_{out}+$ and sets the common-mode voltage V_{CMFB}. Chopper modulators chn(chp) are used to modulate the 1/f noise from M_{P1} – M_{P8} and M_{N1}- M_{N4} and control clocks ϕ_m and ϕ_m' follows Fig. 4(c) [20].DDA achieves a simulated open-loop gain of 106 dB, phase margin of 62°, an IRN of 1.8μV, and a unity-gain frequency of 32kHz, resulting in a closed-loop bandwidth of 800 Hz while dissipating 1.2 μA from a 1.8-V supply. Super class-AB output stage provides 36-dB gain and an output impedance R_{out} = 120kΩ which is a few orders of magnitude lower than conventional class-AB output stages [20].

V. CONCLUSION

This work provides a comprehensive analysis of the GMR sensor-based analog front-end design in a low-voltage environment. Combining 'COMSOL' SPICE environment reduces the design complexity, improves the design accuracy, and dictates the AFE gain range. The DDA of AFE is implemented in a 180 nm, 1.8 V process. The DDA achieves a closed-loop gain of 32 dB and bandwidth of 800 Hz while dissipating 2.16 μW.

REFERENCES

[1] V. K. Chugh, K. Kalyan, Anoop C. S., A. Patra and S. Negi, "Analysis of a GMR-based plethysmograph transducer and its utility for real-time Blood Pressure measurement," *2017 39th Annual International Conference of the IEEE Engineering in Medicine and Biology Society (EMBC)*, Jeju, Korea (South), 2017, pp. 1704-1707.

[2] J. R. Bai and V. J. Kumar, "Optimal Design to Ensure Maximum Coupling Between Magnetic Flux and Arterial Blood in a Magneto Plethysmo Gram Sensor Head," in *IEEE Sensors Journal*, vol. 21, no. 2, pp. 1417-1423, Jan.15, 2021.

[3] J. R. Bai and V. J. Kumar, "Use of Magneto Plethysmogram Sensor for Real-Time Estimation of Hemoglobin Concentration," in *IEEE Sensors Journal*, vol. 21, no. 4, pp. 4405-4411, Feb.15, 2021

[4] S. Dutta, T. Sen and C. S. Anoop, "Study and Noise Analysis of a Linearizing Front-End Circuit for GMR Sensors," *2019 IEEE Region 10 Conference (TENCON)*, Kochi, India, 2019, pp. 2275-2279.

[5] T. Sen, C. S. Anoop, and S. Sen, "Design and performance evaluation of two novel linearization circuits for giant magnetoresistance based sensors," *IET Circuits, Devices Syst.*, vol. 11, no. 5, pp. 496–503, 2017.

[6] T. Sen, C. S. Anoop, and S. Sen, "Simple linearising front-end-circuit for giant magnetoresistance sensors," *Electron. Lett.*, vol. 54, no. 2, pp. 81–83, 2018.

[7] T. Sen, A. Maity, and S. Sen, "On-Chip Implementation of Analog Linearization Schemes for Giant-Magnetoresistance Sensors," *2018 12th Int. Conf. Sens. Technol.*, pp. 419–423, 2018.

[8] C. T. Phua, "Novel method of blood pulse and flow measurement using the disturbance created by blood flowing through a localized magnetic field," *Phd. Thesis*, p. 1-214, 2012.

[9] J. R. Bai, S. Mohanasankar, V. J. Kumar, "Motion Artifact-Free Magnetoplethysmogram," *2018 9th Cairo Int. Biomed. Eng. Conf.*, no. 3, pp. 78–81, 2018.

[10] https://www.nve.com/Downloads/analog catalog.pdf

[11] H. Chaudhary, S. Kodge and M. Sharad, "Digitally assisted analog processing unit for MPG based wearable device," *2017 IEEE 60th International Midwest Symposium on Circuits and Systems (MWSCAS)*, Boston, MA, 2017, pp. 257-260.

[12] A. Mohamed, M. Schmid, A. Tanwear, H. Heidari and J. Anders, "A Low Noise CMOS Sensor Frontend for a TMR-based Biosensing Platform," 2020 *IEEE Sensors*, Rotterdam, Netherlands, 2020, pp. 1-4.

[13] K. Kalyan, V. K. Chugh and C. S. Anoop, "Non-invasive heart rate monitoring system using giant magneto resistance sensor," *2016 38th Annual International Conference of the IEEE Engineering in Medicine and Biology Society (EMBC)*, Orlando, FL, 2016, pp. 4873-4876.

[14] C. Sawigun and S. Thanapitak, "A Compact sub μW CMOS ECG Amplifier With 10GΩ Rin, 2.02 NEF, 8.16 PEF and 83.24-dB CMRR," in *IEEE Transactions on Biomedical Circuits and Systems*, (Early access)

[15] J. Oreggioni, A. A. Caputi and F. Silveira, "Current-Efficient Preamplifier Architecture for CMRR Sensitive Neural Recording Applications," in *IEEE Transactions on Biomedical Circuits and Systems*, vol. 12, no. 3, pp. 689-699, June 2018.

[16] C. Cabrera, R. Caballero, M. C. Costa-Rauschert, C. Rossi-Aicardi and J. Oreggioni, "Low-Voltage Low-Noise High-CMRR Biopotential Integrated Preamplifier," in *IEEE Transactions on Circuits and Systems I*:Regular Papers, vol. 68, no. 8, pp. 3232-3241, Aug. 2021

[17] S. Zuo, K. Nazarpour and H. Heidari, "High-Precision Biomagnetic Measurement System Based on Tunnel Magneto-Resistive Effect," 2020 *27th IEEE International Conference on Electronics, Circuits and Systems (ICECS)*, Glasgow, Scotland, UK, 2020, pp. 1-4.

[18] S. Zuo, H. Fan, K. Nazarpour and H. Heidari, "A CMOS Analog Front-End for Tunnelling Magnetoresistive Spintronic Sensing Systems," *2019 IEEE International Symposium on Circuits and Systems (ISCAS)*, Sapporo, Japan, 2019, pp. 1-5.

[19] Y.P.Hsu, Z. Liu and M. M. Hella, "A 12.3-μW 0.72-mm² Fully Integrated Front-End IC for Arterial Pulse Waveform and ExG Recording," *IEEE Journal of Solid-State Circuits*, vol. 55, no. 10, pp. 2756-2770.

[20] Y. Zhao, Z. Shang, "A 2.55 NEF 76 dB CMRR DC-Coupled Fully Differential Difference Amplifier Based Analog Front End for Wearable Biomedical Sensors," in *IEEE Transactions on Biomedical Circuits and Systems*, vol. 13, no. 5, pp. 918-926, Oct. 2019.

[21] P. R. Kinget, "Device mismatch and tradeoffs in the design of analog circuits," in *IEEE Journal of Solid-State Circuits*, vol. 40, no. 6, pp. 1212-1224, June 2005.

[22] S. Sarkar, "Design of Magnetic Sensor Based All-in-One Cardiorespiratory Health Monitoring System," 2020 42nd Annual International Conference of the IEEE Engineering in Medicine Biology Society (EMBC), 2020, pp. 4660-4663.